IOP Publishing Smart Materials and Structures
Smart Mater. Struct. 27 (2018) 115014 (15pp) https://doi.org/10.1088/1361-665X/aadfac

Actuation performance of fluidic origami cellular structure: a holistic investigation

Hrishikesh Sane[1], **Priyanka Bhovad**[1] **and Suyi Li**

Department of Mechanical Engineering, Clemson University, Clemson, SC United States of America

E-mail: suyil@clemson.edu

Received 15 May 2018, revised 31 August 2018
Accepted for publication 7 September 2018
Published 15 October 2018

Abstract

Motivated by the sophisticated geometries in origami folding and the fluidic actuation principle in nastic plant movements, the concept of fluidic origami cellular structure was proposed for versatile morphing and actuation. The idea is to assemble tubular Miura-ori modules into a cellular architecture, and apply fluidic pressure to induce folding and hence actuation. Despite the promising potentials, the actuation capabilities of fluidic origami, such as free stroke and block force, are not elucidated. In particular, the effects of the thick facet material stiffness and pressure-sealing end caps are not understood. These gaps in our knowledge prevent the practical implementations of fluidic origami. Therefore, this study aims to address these issues by incorporating realistic considerations into the design, fabrication, and analysis of fluidic origami. We construct CAD models of the fluidic origami modules based on realistic design parameters to ensure that they can be fabricated via commercially accessible 3D printers while remaining pressure proof. We then use both simplified analytical methods, such as the equivalent truss frame model, and the more comprehensive finite element methods to examine the actuation performance. Comparing the results from these different methods can reveal the influences of end caps and thick facet material stiffness. Based on these insights, a customized generic algorithm is used to identify the optimal fluidic origami designs for fluidic actuation. It is found that an optimal folding angle exists to maximize the actuation capability, while the sector angle of Miura-ori can be tailored to effectively program the actuation performance.

Keywords: origami, bio-inspiration, morphing and actuation

(Some figures may appear in colour only in the online journal)

1. Introduction

Over the past several decades, the art of origami paper folding has been transformed into a design and fabrication framework for developing different sheet materials into sophisticated 3D shapes [1–3]. As a result, we are witnessing the rapid emergence of origami-inspired engineering applications spanning from the large-scale deployable aerospace structures [4, 5], kinetic architectures [6, 7], and self-reconfigurable robots [8, 9] to the small-scale biomedical devices [10], mechanical metamaterials [11–13], and DNA machines [14]. These applications leverage the folding-induced shape reconfiguration to achieve their target performance, which can be tailored with an exceptionally large freedom by carefully designing the underlying crease patterns [15, 16]. This advantage is especially evident if the crease pattern is *rigid-foldable*, so that one can analyze the shape reconfiguration by treating the origami facets as rigid panels revolving around hinge-like crease lines—essentially a 3D linkage mechanism.

The versatile shape reconfiguration capability of origami is especially appealing for embedded actuation because folding can be used to program sophisticated actuation motion paths. Therefore, a *fluidic origami cellular structure* concept (referred simply as 'fluidic origami' hereafter) was proposed by the authors via combining the origami geometry and the actuation principles of plant nastic movements [17]. Fluidic origami is essentially an assembly of *tubular modules* consisting of carefully designed, rigid-foldable Miura-ori sheets (figure 1). When these modules are pressurized either pneumatically or hydraulically, they fold and generate effective

[1] Equal contribution.

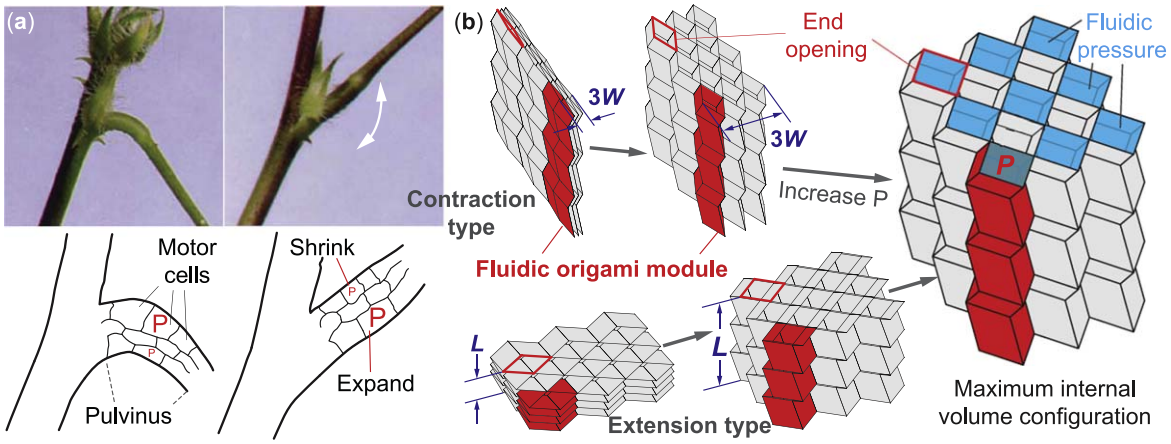

Figure 1. The concept of plant-inspired fluidic origami cellular structure. The nastic movements in plants (a) and fluidic origami (b) share the similar working principle: That is, the embedded and distributed pressurization in the cellular structure can enable versatile actuation motion. In the mimosa plant shown in (a), increase or decrease the turgor pressure can expand or shrink motor cells to bend the leaves. (Image adopted from [28] with permissions) In the fluidic origami shown in (b), an increasing internal fluidic pressure can induce large amplitude folding and generate actuation motion in both *L* and *W* directions. Note that the folding kinematics shown in this figure is based on idealistic model assuming rigid-folding, and the opening at the two ends of the fluidic origami modules changes their shapes significantly.

actuation motion until the maximum internal volume allowed by rigid-folding is reached. Such a distributed, pressure activated actuation shares similar working principles to the rapid nastic movements in plants like *Mimosa pudica*, which can selectively manipulate the turgor pressure in its motor cells to create an internal bending moment for leaf folding [18, 19] (figure 1(a)). Compared to other plant-inspired, pressure activated cellular structure concepts such as PACS [20], pressure adaptive honeycombs [21], and topologically optimized trailing edge [22, 23]; the fluidic origami has some unique advantages. Firstly, folding is a fundamentally three-dimensional shape reconfiguration that can enable complex motions like a combined extension and shear [13]. Secondly, the pressurized fluidic origami modules can be seamlessly integrated with non-pressurized origami sheets for large-scale and efficient motions. Finally, the morphing and actuation capability of fluidic origami can be complemented by other adaptive functions such as stiffness adaptation [17] and pressure-dependent multi-stability [24]. The stiffness adaptation, which can be achieved near instantaneously via simple on/off valve control, can reduce the power requirements for actuation without sacrificing the external load bearing capacity. Meanwhile, the multi-stability can significantly amplify the actuation speed and magnitude similar to the impulsive trap closing motions in *Venus flytrap* [25]. Therefore, fluidic origami has great potentials to advance state-of-the-art of many engineering systems that require embedded actuation such as morphing airframe [26] and soft robots [27].

Despite these promising potentials, the actuation capabilities of fluidic origami such as free stroke and block force are not yet fully elucidated. Especially, previous studies by the authors relied on idealistic models assuming that (1) the origami facets have zero thickness, (2) the crease lines act like simple hinges, and (3) the tubular modules are sealed by ideal end caps that can perfectly accommodate the shape changes of their end openings. Indeed, similar assumptions have been made by many other studies on origami-inspired structures and materials. These idealistic models can reveal the working principles without unnecessary complexities, but they inevitably neglected many important factors in practical implementations. In particular, additive manufacturing or 3D printing is considered as one of the most viable approaches to fabricate the complex geometries of multi-cellular fluidic origami while maintaining internal pressure sealing. Thus the finite thickness and compliance of the 3D printed facet and crease materials must be considered in order to examine the realistic actuation performance of fluidic origami. Furthermore, a realistic pressure-sealing end cap at the end openings of fluidic origami module can be incompatible with the folding-induced shape changes (figure 1). Therefore, end caps can reduce the actuation performance and such negative effects must be analyzed carefully.

Therefore, the objective of this study is to conduct a holistic investigation of the actuation performance of the fluidic origami by incorporating realistic considerations in its design and fabrication. This study is conducted based on the CAD models of fluidic origami modules featuring finite facet material thickness and flat end caps. Various design variables, such as the material thinning along the crease lines, are carefully chosen to ensure that the fluidic origami modules can be fabricated via commercially accessible 3D printing machines. Two types of modules are designed based on their initial folding configurations, one contracts along longitudinal *L* direction under pressurization, and the other extends. Based on these CAD designs, we examine the free stroke and block force of fluidic origami module using two different approaches. The first approach relies on the simplified models used in authors' previous publication [17] and many other studies on origami-inspired engineering applications; and the second approach uses the more comprehensive finite element simulations. Comparing the results from these two different approaches can reveal the correlations between the fluidic origami actuation performance and many practical design considerations including Miura-ori geometry, facet thickness,

material stiffness, and end caps. And understanding these correlations will eventually enable us to identify the optimal fluidic origami design. Therefore, this study can provide the practical guidelines for implementing fluidic origami as an active and adaptive structure.

The rest of this paper is organized as follows. Section 2 discusses the design, kinematics, and fabrication of the fluidic origami module. Sections 3 and 4 contains the in-depth analysis of its free stroke and block force performance, respectively. These two sections also include parametric analyses revealing the correlation between the actuation performance and the underlying Miura-ori design. Section 5 discusses an optimization of the fluidic origami design for a balanced actuation capability. Section 6 concludes this paper with summaries and discussions.

2. Design and fabrication of the fluidic origami module

2.1. Miura-ori design and folding kinematics

The backbone of a fluidic origami module consists of two identical Miura-ori strips connected along their zig-zag crease lines (figure 2(a)). The design, stacking, and folding kinematics of the Miura-ori sheets have been extensively discussed in previous studies [11, 13, 29]. Here we only provide a brief overview for clarity. Miura-ori design is determined by three variables that remain unchanged regardless of folding: they are the crease length a, b and the sector angle γ between them. To describe the amount of folding, a folding angle θ is introduced as half of the dihedral angle between adjacent facets of the two connected Miura-ori strips (figure 2(a)). According to rigid-folding kinematics that assumes rigid facets, hinge-like crease lines, and ideal end caps, the folding angle can take any values from 0° to 90° (figure 2(b)). $\theta = 0°$ indicates that the Miura-ori is flat, and $\theta = 90°$ means it is fully-folded. The correlations among the external length L, width W, enclosed internal volume V, and the folding angle θ are strongly nonlinear as follows [30],

$$L = \frac{2nb\cos\theta\sin\gamma}{\sqrt{1-\sin^2\gamma\sin^2\theta}}, \tag{1}$$

$$W = 2a\sin\theta\sin\gamma, \tag{2}$$

$$V = na^2b\sin^2\gamma\sin(2\theta), \tag{3}$$

where n is the number of Miura-ori unit cells—the most elementary geometric identity—along the length of a tubular fluidic origami module. For example, the module shown in figure 2 has three unit cells so $n = 3$. Clearly, the maximum volume always occurs when $\theta = 45°$ regardless of the Miura-ori design; and this is the critical, locking configuration at which further pressurization could not induce more actuation motion. Therefore, we can define two types of fluidic origami modules based on their initial *resting folding angle* $\theta°$. The first type, which features a resting folding angle less than 45°, slightly contracts in length L but significantly expands in width W under internal pressurization until the maximum volume configuration is reached (figure 1(b)). For clarity, it will be referred as the 'contraction type' hereafter. The second type of fluidic origami module has a resting folding angle bigger than 45°, so it extends significantly in length L but slightly contracts in width W (figure 1(b)). We will refer it as the 'extension type'.

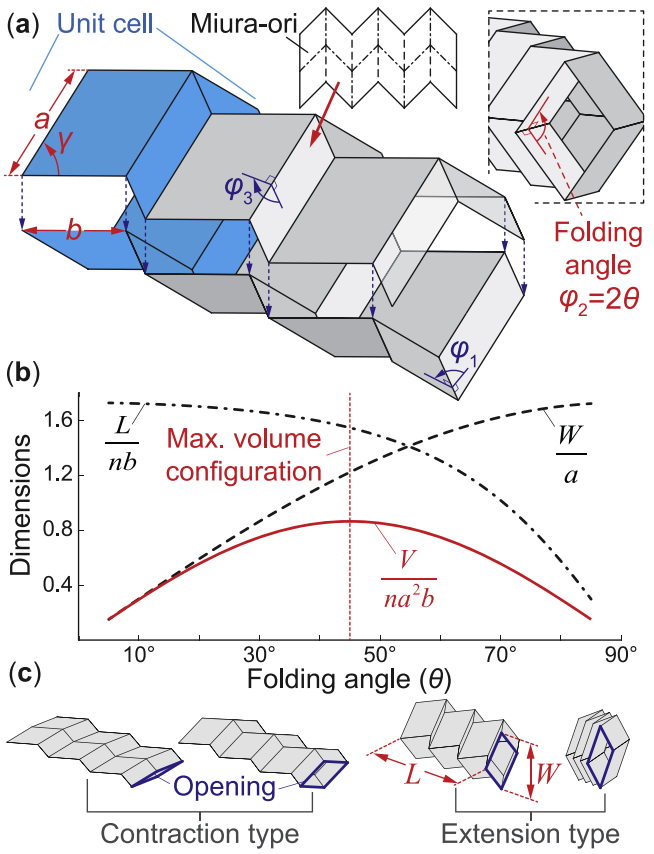

Figure 2. Design and ideal rigid-folding kinematics of a fluidic origami module. (a) A module consists of two identical Miura-ori strips connected along their crease lines. The most elementary unit cell and its important design parameters are highlighted. This particular module has three unit cells. The inserted figure at the top right illustrates the definition of folding angle θ. (b) The relationships among the folding angle, normalized length, width, and the internal enclosed volume according to the rigid-folding kinematics. In this figure $\gamma = 60°$. (c) Folded fluidic origami modules corresponding to $\theta = 5°$, 25°, 65°, and 85° from left to right. Notice that the end opening of the fluidic origami exhibits significant shape changes.

2.2. Additional design variables for fabrication by 3D printing

Practical implementation of the fluidic origami requires additional design parameters, and the facet thickness is one of the most important ones to consider. Several methods of customizing the crease pattern for thick facets have been proposed [7, 31], but they are not intended for 3D printing. In this study, we introduce the facet thickness t_F by inward offsetting from the Miura-ori backbone geometry defined in equations (1)–(3) (figure 3(b)). In this way, pressure-proof fluidic origami modules can be 3D printed and seamlessly integrated into a multi-cellular structure. However, such offsetting method would also generate excess amount of

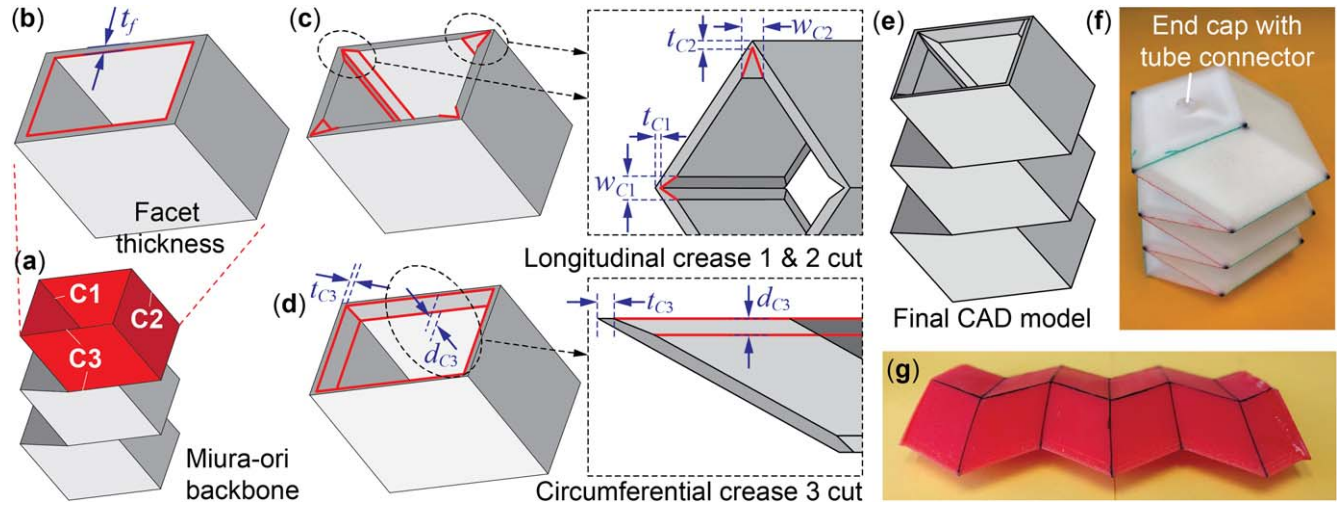

Figure 3. CAD design and 3D printing of the fluidic origami modules. (a, b) The facet thickness is modelled by an inward offsetting from the Miura-ori backbone geometry. (c, d) V-grooves are added along the crease lines to facilitate proper folding. (e) A finished CAD model for the fluidic origami module that includes the facet thickness and all crease thinning. This model was then sent directly to the 3D printers. (f) SLS printed, extension type of fluidic origami module using PEBA materials. (g) FDM printed contraction type of fluidic origami using TPU materials. Flat end caps are printed separately and glued to provide proper pressure sealing.

materials along the crease lines and hinder proper folding, because the material bending stiffness along the creases needs to be significantly smaller than that of the facets. To address this issue, the material thickness along the crease lines is reduced by introducing v-grooves. Dimensions of these v-grooves are defined differently for different creases. Along the *longitudinal* creases that are labeled as $C1$, $C2$ in figure 3, the v-grooves are defined by the width at the opening w_{C1}, w_{C2} and the minimum crease thickness t_{C1}, t_{C2} (figure 3(c)). Here the v-groove geometries need to be designed differently because $C1$ and $C2$ creases have different dihedral opening angles. The thinning of the *circumferential* creases $C3$ is achieved by offsetting from the Miura-ori backbone by a thickness of t_{C3} and then applying a tapered cut at the depth of d_{C3} (figure 3(d)). Such design variable setup is chosen to minimize the geometric incompatibilities in the optimization discussed later in section 5. Moreover, the crease cannot be too thin otherwise it would be impractical for 3D printing and pressure proofing. A minimum of 1 mm of crease thickness is found to be reasonable after repeated trials and errors. Two fluidic origami prototypes are fabricated to validate the manufacturability, and their design values are summarized in table 1. One prototype is of extension type, and it is made of an elastoplastic material called polyether block amide (PEBA) on a selective laser sintering printer (SLS, fabricated by Shapeways Inc., figure 3(f)). The other prototype is of contraction type, made of a thermoplastic polyurethane (TPU) material on a fused deposition modeling (FDM) printer (LulzBot TAZ 5, figure 3(g)). Both materials feature superior flexibility with more than 100% of elongation at break. The SLS procedure based on the PEBA material can produce more accurate fluidic origami geometries without the need of support materials, which can be very challenging to be removed after printing. The FDM based on TPU material, on the other hand, is significantly cheaper and more accessible but careful CAD designs are necessary to reduce the use of support materials as much as possible. In addition, the printing specifications of FDM must be setup appropriately to minimize pressure leakage through the interface between adjacent material layers. After repeated trials and errors, we found 0.1 mm of layer height, 100% of fill density, 15 mm s^{-1} of print speed, 220 °C of nozzle temperature and 85 °C of bed temperature can produce high quality TPU fluidic origami. End caps are separately 3D printed and glued to the module. They are designed to be flat and fit the end openings at initial resting configuration. Therefore, the shapes of end caps are different for different origami designs.

Table 1. Design parameters of the two fluidic origami prototypes shown in figure 3.

Design Parameter		Extension	Contraction
Miura-ori backbone geometry	a	62.5 mm	46.9 mm
	b	50 mm	37.5 mm
	γ	60°	60°
	$\theta°$	70.5°	16.1°
	n	3	3
Additional design variables	t_F	4 mm	3 mm
	t_{C1}	2 mm	1.5 mm
	t_{C2}	1 mm	4.5 mm
	w_{C1}	8 mm	7.5 mm
	w_{C2}	8 mm	1.5 mm
	t_{C3}	2 mm	2.3 mm
	d_{C3}	3 mm	2.6 mm

2.3. Testing the hyperelastic property of the 3D printed PEBA and TPU materials

Mechanical properties of the 3D printed PEBA and TPU material are quite sensitive to the aforementioned printing specifications. Thus it is necessary to accurately measure their

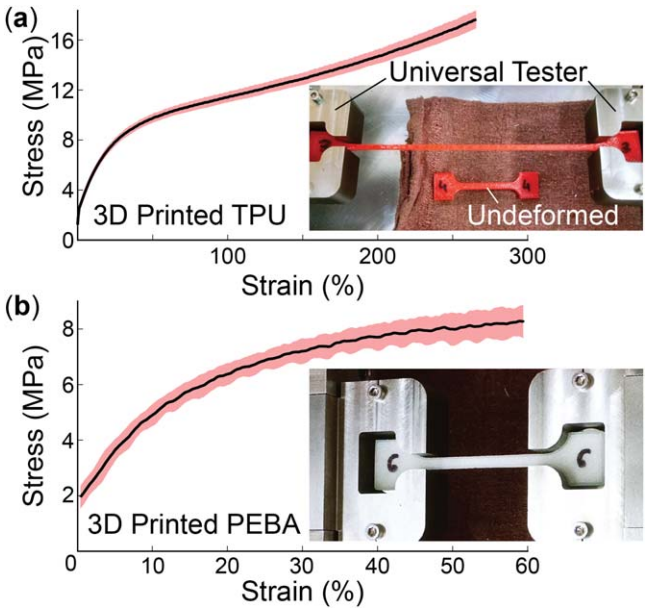

Figure 4. Testing the hyperelastic properties of the 3D printed TPU (a) and PEBA materials (b). The solid curve is the averaged results based on six dog bone samples, and shaded bands are the standard deviation.

hyperelastic properties for the subsequent finite element analyses and design optimization. Dog bone specimens were fabricated based on the same printing specifications as the fluidic origami prototypes (figure 4(a)). They are made referring to the ASTM D638 standards, and have the dimensions of 3 mm in thickness, 4.3 mm in width, and 30 mm in length. Displacement controlled tensile tests are conducted on these dog bone specimens (Modular under Microscope Mechanical Test System-μTS, Psylotech; 300 μm s^{-1} displacement rate for TPU samples and 50 μm s^{-1} for PEBA samples; approximately 250% of strain). The averaged test results shown in figure 4 exhibit a typical nonlinear and hyperelastic material behavior. The mooney-Rivlin five parameter material model in ANSYS™ is used to curve fit the experiment results over the entire tested displacement range, and the fitted material parameters are listed in table 2.

Table 2. Fitted mooney-Rivlin 5 parameters. They are used in finite element simulations hereafter, and the units are all in MPa.

	TPU	PEBA
C_{10}	−37.75	−56.45
C_{01}	51.89	71.47
C_{20}	0.79	1.50
C_{11}	−4.59	−10.34
C_{02}	17.79	32.59

3. Free stroke performance of the fluidic origami

Free stroke and block force are the two most commonly used performance metrics for actuators. In this study, the free stroke S of the fluidic origami module is defined as the ratio of its averaged extension or contraction due to internal pressure over its initial dimensions, while no external loads are applied. For effective actuation, we examine the longitudinal deformation of the extension type of fluidic origami and transverse deformation of the contraction type. That is, $S = X_{\text{final}}/X_{\text{initial}} - 1$, where $X = L$ for the extension type and $X = W$ for the contraction type. The free stroke of fluidic origami is a function of internal pressure, and its magnitude increases monotonically with increasing pressure until the maximum volume configuration is reached. Moreover, since the free stroke is associated to folding, its magnitude is dictated by the torsional stiffness of creases. We investigate the free stoke of fluidic origami based on two different approaches. The first approach in section 3.1 is more simplistic, assuming rigid facets and ideal end caps, similar approaches have been used extensively for other rigid-foldable origami research. The second approach in section 3.2 is based on finite element simulation using practical design considerations such as the facet thickness and realistic end caps. Comparing the results from these two approaches can offer us a comprehensive understanding of the free stroke performance. In section 3.3, we further conduct a parametric study to reveal the correlation between free stoke and underlying Miura-ori designs.

3.1. Simplified approach for free stroke analysis

In this approach, we assume ideal end caps that can seal the internal pressure without hindering the shape changes of the end opening. In this way, the pressure-induced deformations of fluidic origami follow the rigid-folding kinematics defined in equations (1)–(3), and the corresponding total energy can be approximated as the summation of crease strain energies and the work done by pressure:

$$U_t = \Pi_c + W_P = \sum_i \frac{1}{2} k_i^c (\varphi_i - \varphi_i^o)^2 - P(V - V^o), \quad (4)$$

where φ_i and k_i^c are the dihedral opening angles and torsional stiffness of the crease lines, respectively (figure 2(a)). $\varphi_1 = \pi - 2\theta$, $\varphi_2 = 2\theta$, and $\varphi_3 = 2\sin^{-1}[\cos\theta(1 - \sin^2\theta\sin^2\gamma)^{-1/2}]$. φ_i^o and V^o are initial crease angles and enclosed volume corresponding to the resting folding angle $\theta°$. The folding angle at a given internal pressure can be calculated by solving the following equation based on virtual work principle,

$$\sum_i k_i^c (\varphi_i - \varphi_i^o) \frac{\mathrm{d}\varphi_i}{\mathrm{d}\theta} - P\frac{\mathrm{d}V}{\mathrm{d}\theta} = 0. \quad (5)$$

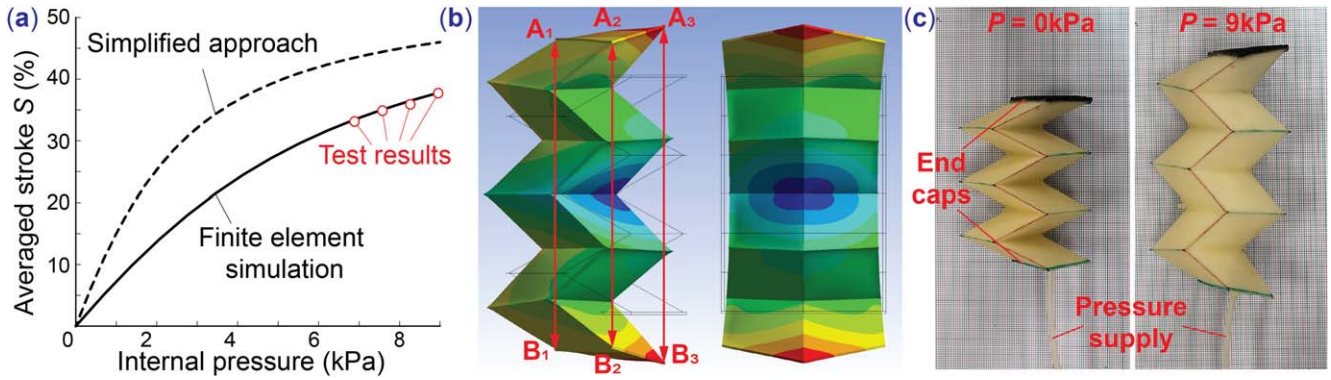

Figure 5. Free stroke analysis of the extension type of fluidic origami prototype along the length direction. (a) Free stroke performance based on the simplified approach, FEA, and experimental measurements. (b) FEA results showing the deformation pattern of the whole module. The 'bending' at the two ends of the module is the result of kinematic incompatibility between the flat end cap and shape change due to folding. The effective stroke is measured as the averaged extension between the nodal points A_i and B_i, (i = 1, 2, and 3). (c) 3D printed fluidic origami prototypes under pressurization. There are good agreements between FEA and experiments in terms of deformation pattern and the averaged free stroke. In this paper, the color map in the FEA results represents the nodal displacements.

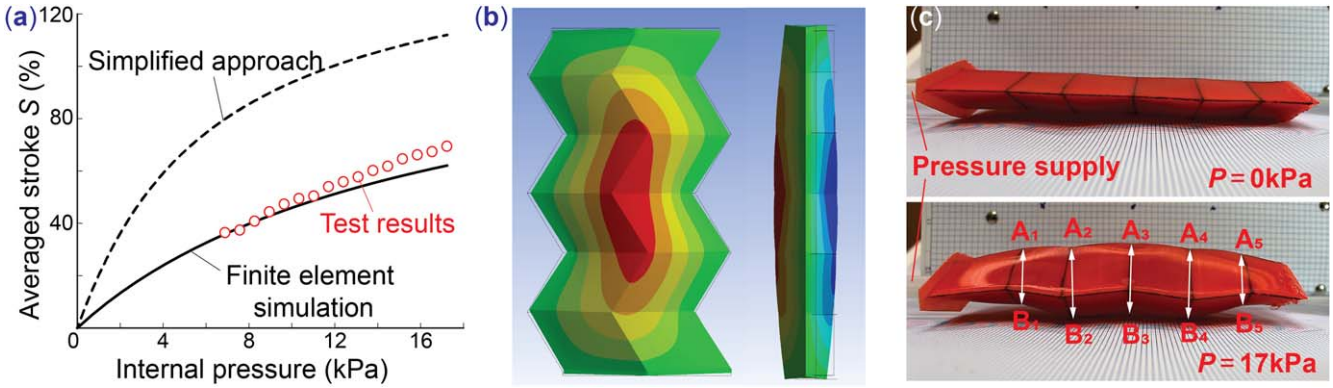

Figure 6. Free stroke analysis of the contraction type of fluidic origami prototype along its width direction. (a) Free stroke performance based on the simplified approach, FEA, and experimental measurements. (b) FEA results of the whole module, and (c) the experiments. In this case, the free stroke is measured as the averaged displacement between nodal points A_i and B_i (i = 1, 2 … 5).

The solution of θ can be inserted into equations (1) or (2) to calculate the free stroke. It is evident from equations (4) and (5) that the free stroke performance is directly related to the crease torsional stiffness k_i^c in that stiffer crease lines will reduce the free stroke at a given pressure level. The crease torsional stiffness estimation for the 3D printed extension and contraction fluidic origami prototypes are detailed in appendix A.1. The calculated free stroke magnitude with respect to pressure are shown as the dashed curves in figures 5(a) and 6(a).

3.2. Finite element approach and experimental validation

For considering the effects of facet material thickness and realistic end caps, the simple mechanics model based on rigid-folding kinematics is no longer sufficient and finite element method (FEA) is necessary. We conduct finite element analyses directly on the same CAD models used for prototype 3D-printing and the results are shown in figures 5(a), (b) and 6(a), (b) (ANSYS™, SOLID 186 and SOLID187 element). For the extension type of fluidic origami module, the flat end caps are incompatible with the folding-induced shape changes of its end openings, as a result, the single unit-cell at each ends of the fluidic origami module exhibits a complex bending deformation so that the endcaps rotate with respect to their original positions. The free stroke, defined based on the averaged displacement between the end caps, is reduced significantly compared to the results from the simplified approach (figure 5(a)). The end caps in the contraction type of fluidic origami module also constrain the folding motion and reduce the corresponding averaged free stroke (figure 6(a)).

To validate the end cap effects predicted by the finite element analyses, free stroke responses of the two 3D-printed fluidic origami prototypes are experimentally tested. Digitally controlled DC voltage-pressure converter (OMEGA™ E/P510 converter with TENMA 72-2690 power supply) is used to supply pneumatic pressure to the fluidic origami prototype, while its deformations at different pressure levels are captured by high-resolution camera (CANON EOS Rebel T5i). The free stroke magnitudes are measured by using the MATLAB image processing toolbox (figures 5(c) and 6(c)). The experimentally measured deformation pattern and averaged free stroke agree well with the FEM predictions. Therefore, we can use the finite element methods to conduct further parametric investigations.

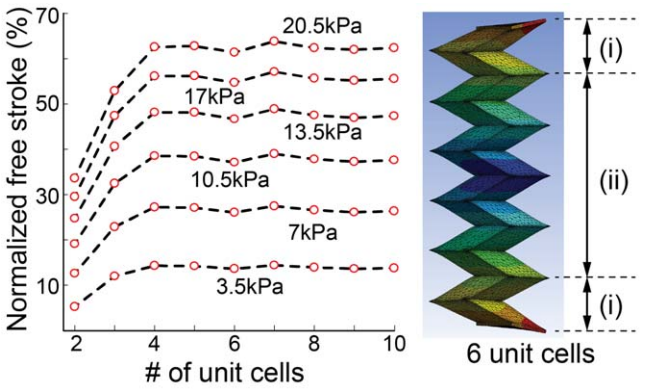

Figure 7. Free stroke performance vs. the number of unit cells in a fluidic origami module. (i) The single unit cell at each end of the fluidic origami module exhibits complex bending due to end caps; and (ii) the unit cells in the middle deform according to the kinematics of rigid-folding described in equations (1) and (2).

Another important observation from the FEA is that, regardless of the underlying Miura-ori designs, the end cap effects seem to be confined only to the single unit cell at each ends of the fluidic origami modules, and the deformation of the unit cells in the middle is consistent with the rigid-folding kinematics. To verify this, we conduct further finite element analysis on the extension type of fluidic origami consisting of different number of unit cells using TPU material properties. The simulation results, shown in figure 7, confirm this observation because the normalized free stroke converges as the number of unit cells exceeds three. It is worth noting here that if the end caps are designed to be non-flat, their deformation would be different. Indeed, a different study suggests that carefully designed non-flat end caps can better accommodate the deformation of pressurized cellular structures like the fluidic origami [32]. Nonetheless, optimizing the shape of end cap is beyond the scope of this study.

3.3. Correlation between free stroke and underlying Miura-ori design

A unique advantage regarding fluidic origami is the possibility to program its actuation performance by tailoring the underling Miura-ori design variables. According to the rigid-folding kinematics, the normalized free stroke is only related to the sector angle γ and folding angle θ, therefore, we conducted parametric analyses to examine the correlations between the free stroke in length direction and these two crucial design parameters using TPU material properties. Both the simplified rigid-folding approach and the finite element approach are used, and their results are compared in figure 8. In this parametric analysis, other design parameters such as the crease line lengths and thinning parameters are chosen from a set of baseline designs listed in table 3, and the internal pressure P is set at 34.5 kPa.

By carefully examining the results from this parametric study and the experiment results discussed in previous two subsections, we can come to the following conclusions regarding free stroke performance. (1) The extension type of

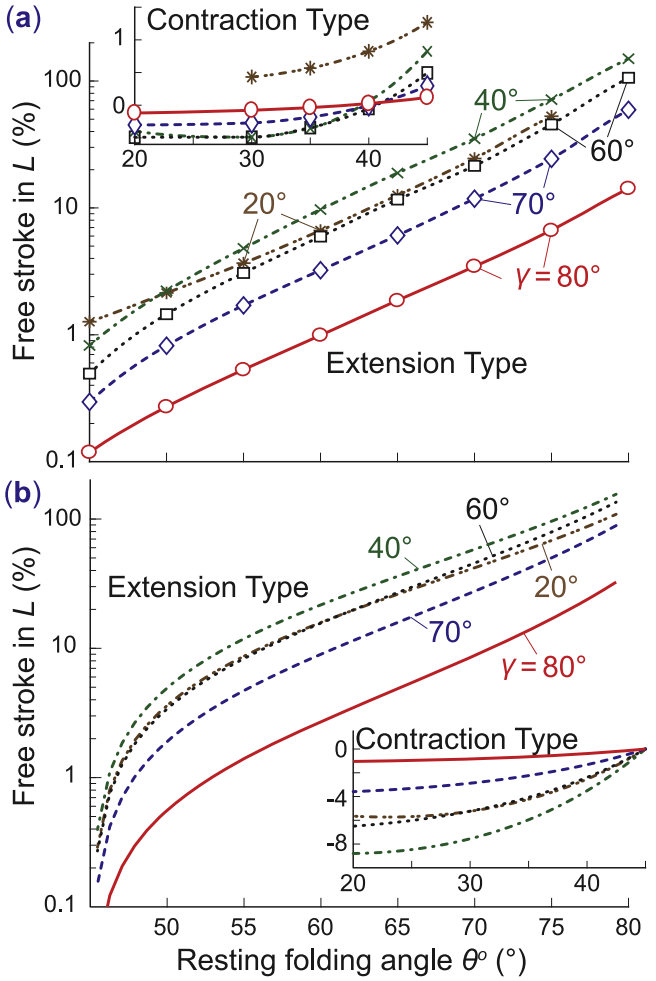

Figure 8. Parametric analyses illustrating the correlation between free stroke performance, the sector angle γ, and resting folding angle θ^o of the underlying Miura-ori. (a) Results from the finite element analysis, where each maker is a simulation result. (b) Results based on the rigid-folding kinematics model. In both (a) and (b), the main figures show the free stroke of the extension type of fluidic origami with $\theta^\circ > 45^\circ$, and the small insert figures show those of contraction type. Note that the vertical axes are in logarithmic scale in the main figures and linear scale in the inserted small figures.

Table 3. Baseline designs used in the parametric analyses in sections 3.3 & 4.3 and the optimization in section 5.

Miura-ori backbone		Crease thinning	
a	31 mm	t_{C1}	1 mm
b	25 mm	t_{C2}	1 mm
γ	60°	w_{C1}	4 mm
θ^o	78°	w_{C2}	4 mm
n	4	t_{C3}	1 mm
t_F	4 mm	d_{C3}	2 mm

fluidic origami actuators generate significantly more free stoke along the length direction than the contraction type. The simplified model and finite element simulations predict close to 100% of free stroke magnitude from the extension type, but less than 10% from contraction type. (2) Among the extension types of actuators based on different Miura-ori designs, those

with resting folding angle close to 90° and sector angle close to 40° provide the largest free stroke. Especially, the free stroke increases monotonically as the resting folding angle θ° increases. (3) The overall trends between free stroke and Miura-ori designs are the same between the results from simplified model and finite element simulation. Therefore, the end caps do not *qualitatively* change the relationship between free stroke and Miura-ori designs; instead, they only reduce the magnitude of the achievable free stroke.

4. Block force performance of the fluidic origami

Block force is another important performance metric because it directly indicates the load carrying capacity of fluidic origami. In this study, block force is defined as the reaction force of the fluidic origami when its stroke is held at zero, that is, the two ends of the fluidic origami are fixed. To examine this performance metric without unnecessary complexities, we only investigate the block force of the extension type fluidic origami in the length direction L using the baseline designs in table 3. We introduce a normalized block force B defined as follows:

$$B = \frac{F}{PA^o}, \tag{6}$$

where F is the magnitude of the block force according to an internal pressurization P, and $A^o = 2a^2 \sin\theta^\circ \sin\gamma\sqrt{1 - \sin^2\theta^\circ \sin^2\gamma}$ is the cross-section area of the fluidic origami at the initial resting configuration. Unlike the free stroke, the block force is more closely related to the facet material stiffness rather than crease torsional stiffness. Therefore in this section, we examine the block force by using two different approaches, the first approach is based on an equivalent truss-frame model that has been used extensively by many other studies on origami-inspired structures and materials [6, 11, 17, 33]. Results of this approach will be discussed in section 4.1. The other approach is finite element simulation and it is discussed in section 4.2. A parametric study is also conducted and discussed in section 4.3.

4.1. Block force analysis based on the truss frame model

The equivalent pin-jointed truss frame model used in this approach essentially converts the continuous origami into a discrete system with a finite degrees of freedom. In this model, the creases are represented by stretchable truss elements, and the facets are triangulated along the short diagonals with additional truss elements to provide a first order estimation of their bending. Torsional spring stiffness are assigned to the dihedral angles defined by the truss elements along the creases and across facets to represent the crease torsional and facet bending stiffness, respectively (figure 9(a)). In this way, the truss frame model can establish the connection between block force and facet compliance while assuming ideal end caps. Three geometric transformation matrices and vectors are necessary for analyzing the

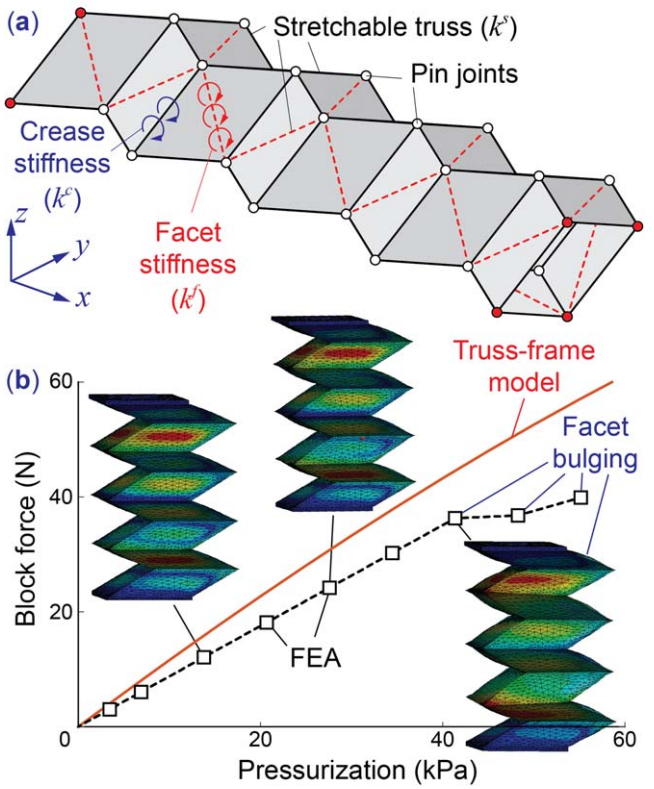

Figure 9. Block force analysis of the fluidic origami. (a) Illustration of the equivalent truss-frame model. The solid lines are truss elements representing the crease lines, and dashed lines are truss elements that triangulate the facets. Pin joints at the ends are highlighted as solid circles, and their displacements along the x-axis are set to zero. (b) Block force and pressure relationship based on the truss-frame model and finite element simulations. From FEA snapshots corresponding to 15 kPa, 30 kPa, and 41 kPa of pressure, one can clearly see the facets bulging out at higher pressure. This indicates a direct relationship between the block force performance and facet material stiffness.

pressure-induced block force based on this truss frame model. They are (1) a compatibility matrix $\mathbf{C}$ correlating the vector of pin-joint displacements $d\mathbf{x}$ to the vector of truss member stretches $\mathbf{e}$ so that $\mathbf{e} = \mathbf{C}d\mathbf{x}$; (2) a transformation matrix $\mathbf{J}$ correlating $d\mathbf{x}$ to the vector of crease angle changes $d\varphi$ so that $d\varphi = \mathbf{J}d\mathbf{x}$; and (3) a row vector $\mathbf{D}$ correlating $d\mathbf{x}$ to the internal volume change dV so that $dV = \mathbf{D}d\mathbf{x}$. The total stiffness matrix $\mathbf{K}$ of the fluidic origami truss frame model is the summation of the facet stretching/shear stiffness $\mathbf{K}^s$ and the bending stiffness $\mathbf{K}^b$. $\mathbf{K}^s$ equals to $\mathbf{C}^T\mathbf{\Lambda}^s\mathbf{C}$, where $\mathbf{\Lambda}^s = diag(k_1^s, k_2^s, \ldots k_n^s)$ is a diagonal matrix containing the equivalent stretch stiffness k_i^s of the truss elements; $\mathbf{K}^b$ equals to $\mathbf{J}^T\mathbf{\Lambda}^b\mathbf{J}$, where $\mathbf{\Lambda}_b = diag(k_1^c, k_2^c, \ldots k_m^c, k_1^f, k_2^f, \ldots k_p^f)$ is a diagonal matrix containing the equivalent crease torsional stiffness k_i^c and facet bending stiffness k_i^f. The derivation of $\mathbf{C}$, $\mathbf{J}$, and $\mathbf{D}$ matrices have been discussed extensively in previous publications [17, 33], and the necessary details for calculating k_i^s, k_i^c, and k_i^f are provided in appendix A.1 for clarity. To analyze the block force while assuming ideal end caps, the longitudinal displacements of the end nodes are

assumed zero, however, their transverse displacements are not constrained (figure 9(a)). The vector of vertices displacement d**x** can be calculated as a function of internal pressure:

$$\mathrm{d}\mathbf{x} = P\mathbf{K}^{-1}\mathbf{D}^{\mathrm{T}}, \tag{7}$$

and the reaction block force can be calculated as the summation of the internal forces from the truss stretches onto the end nodes and the pressure acting on cross-section area at the ends.

4.2. Block force analysis based on finite element simulation

While the equivalent truss frame method can analyze the correlation between facet material stiffness and block force, the finite element model is necessary to incorporate the end cap effects. Figure 9(b) also displays the pressure-block force relationship of the baseline fluidic origami module according to finite element simulations. At low pressure, the block force is linearly proportional to internal pressure, however, the nonlinear finite element simulation predicts that the block force starts to saturate at the higher pressure due to facet bulging.

4.3. Block force vs. Miura-Ori designs

Similar to the free stroke, the block force performance of the fluidic origami module is directly related to the underlying Miura-ori designs, such relationship can be illustrated by the parametric study results in figure 10. The magnitudes of the normalized block force vary significantly as the sector angle γ and resting folding angle θ° change.

By examining the parametric analysis results from both truss frame model and finite elements simulations, we can come to the following conclusions regarding block force performance. (1) Fluidic origami modules with $\gamma = 80^{\circ}$ generates higher block force than other tested sector angles. In particular, those with $\gamma = 40^{\circ}$ perform relatively poorly regarding block force, even though they generate a large free stroke as shown in figure 8. Such a tradeoff between the two actuation metrics will be discussed in detail in the following design optimization. (2) The block force performance peaks when the resting folding angle θ° is designed in the range between 60° and 70°. This is also different from the free stroke analysis results, which recommends a close to 90° resting folding angle for large free stroke. (3) End caps do not qualitatively change the relationships between the block force and Miura-ori designs. However, they significantly reduce the magnitude of achievable block force.

Besides the block force magnitude, another significant difference between the truss-frame model results and FEA simulation is the deformation pattern of fluidic origami. The truss-frame model predicts that the fluidic origami with higher resting folding angle θ° deforms non-uniformly, that is, unit cells at one end of the fluidic origami module contract in the length L direction, while the cells at the opposite end elongate significantly (figure 11). This is because at higher folding angles, the fluidic origami is close to be fully folded; its creases and facets are oriented in a way that can easily

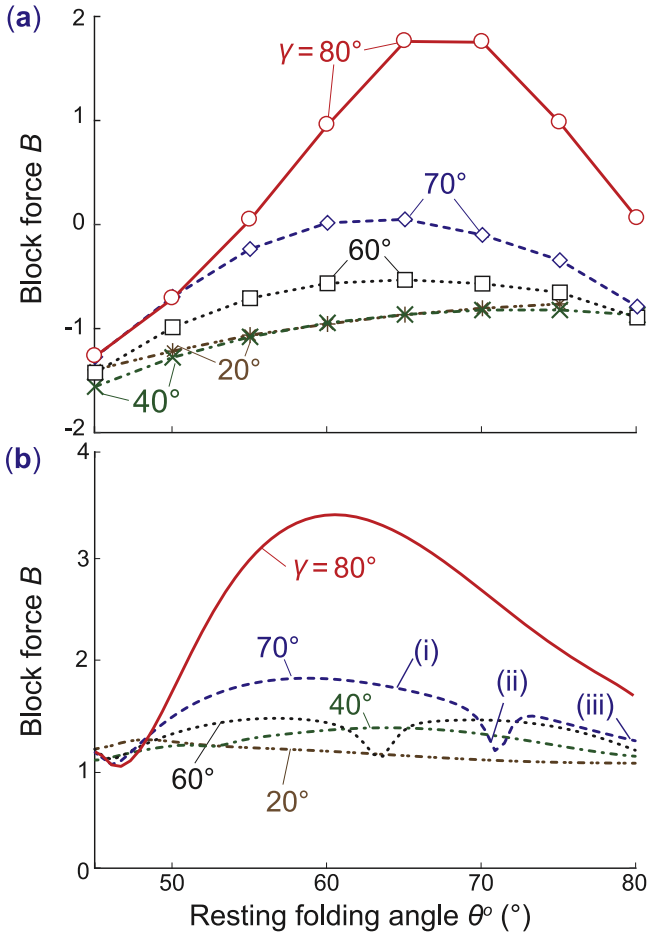

Figure 10. Parametric analyses illustrating the correlations between block force performance, the sector angle γ, and the resting folding angle θ° of the underlying Miura-ori. (a) Results from the finite element analysis, where each maker is a simulation result. (b) Results based on the truss-frame model. Besides γ and θ°, other fluidic origami designs are chosen from table 3, and the pressure is set at 34.5 kPa. Some curves based on the truss-frame model show notable dips regarding the block force magnitude, one of them is labeled by (ii) as an example. These dips are related to the occurrence of non-uniform deformation. Here, (i),(ii), and (iii) are three fluidic origami designs with the same sector angle but different resting folding angles, and their deformation patterns under pressure are shown in detail in figure 11.

accommodate the non-uniform deformations. That is, non-uniform deformations would primarily invoke crease folding without inducing much facet deformations. A similar phenomenon was also studied based on eigenvalue analysis in previous literatures [6, 17], where interested readers can learn more about the underlying physical principles. The finite element results shown in figure 9, on the other hand, do not show such non-uniform deformations. In the truss-frame model, the end caps of fluidic origami module are assumed ideal, that is, they can seal the internal pressure and accommodate the shape changes from folding. Moreover, the facets are assumed to have zero thickness. However in the finite element model, the end caps are no longer ideal and the facets have finite thickness. The non-ideal end caps and thick facets impose additional constraints to the deformation of fluidic

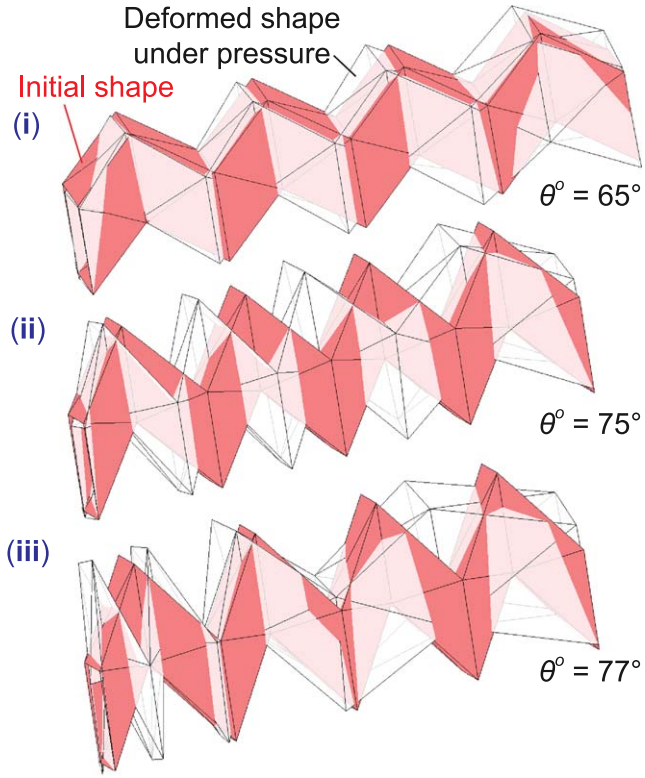

Figure 11. The non-uniform deformation pattern of the fluidic origami based on truss-frame model at 34.5 kPa of internal pressure. All three fluidic origami modules shown here share the same sector angle $\gamma = 70°$, and their corresponding block force performance are labeled in figure 10. It is evident that fluidic origami module with a higher resting folding angle $\theta°$ shows a stronger non-uniform deformation, by which some unit cells contract in their length direction and other cells extend significantly.

origami, preventing the non-uniform deformation from occurring.

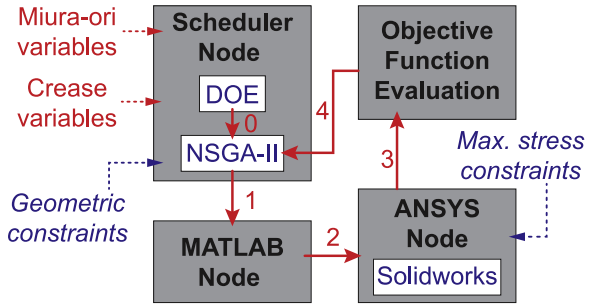

Figure 12. Optimization flowchart. The arrows in the optimization loop stands for (0): design variables of the initial generation of population; (1): design variables of the current generation; (2): CAD modeling parameters of the current generation; (3): finite element simulation results; and (4) the free stroke and block force performance of the current generation. The optimization loop is iterated for 25 generations.

Table 4. Limits of the fluidic origami design parameters used in the optimization. Since the objective functions of free stroke and block force are normalized, the crease line lengths are fixed at $a = 31.25$ mm and $b = 25$ mm in this optimization. Pressure is constant at 34.5 kPa, and the number of unit cells in the fluidic origami module n is 4.

Design Parameter		Minimum	Maximum
Miura-ori backbone	γ	10°	89°
	θ_i	45°	89°
Additional design variables	t_F	0.5 mm	7 mm
	t_{C1}	0.1 mm	7 mm
	t_{C2}	0.1 mm	7 mm
	w_{C1}	0.1 mm	8 mm
	w_{C2}	0.1 mm	8 mm
	t_{C3}	0 mm	7 mm
	d_{C3}	0.1 mm	4 mm

5. Design optimization

Parametric studies discussed in the previous sections clearly indicate that the free stroke and block force performance of the fluidic origami are directly related to the underlying Miura-ori design, and there exists a strong trade-off between these two actuation performance metrics. Therefore, it is necessary to explore the fluidic origami design space more comprehensively. To this end, we conducted a multiple-objective design optimization. This optimization problem is highly nonlinear and involves a large amount of variables, which are listed in tables 1 and 3. Therefore, to identify the globally optimized fluidic origami designs, we use the Non-dominated Sorting Genetic Algorithm II (NSGA-II) available in the modeFRONTIER™ software (2017R1, ESTECO SpA).

Figure 12 illustrates the workflow of the optimization strategy. The 'scheduler node' in this workflow initiates and selects the design variables used in every generation of population. In particular, the initial population is generated by the design of experiment (DOE) part of the scheduler node, which also dictates the design parameters of new generations. This DOE uses the Uniform Latin Hypercube (ULH) method to randomly select designs within a prescribed design space shown in table 4. However, random crease thinning variables can result in geometrically incompatible designs. To mitigate this issue, we combine a set of 26 user-defined, geometrically compatible fluidic origami designs together with 20 randomly assigned designs using ULH to generate the initial population of 46.

The design variables selected by the scheduler node are then sent to the 'MATLAB node,' which runs a customized script file to generate the necessary CAD modeling parameters for the subsequent 'ANSYS node.' This ANSYS node first uses these modeling parameters and a SOLIDWORKS plugin to generate the CAD model, then performs finite element simulations to obtain the normalized free stroke and block force performance. Results of these simulations are then sent back to the scheduler node to generate the design variables of the next generation. Two design constraints are reinforced during the optimization iterations. Firstly, the fluidic origami geometry has to be well-defined for CAD modeling and 3D printing without geometry incompatibility

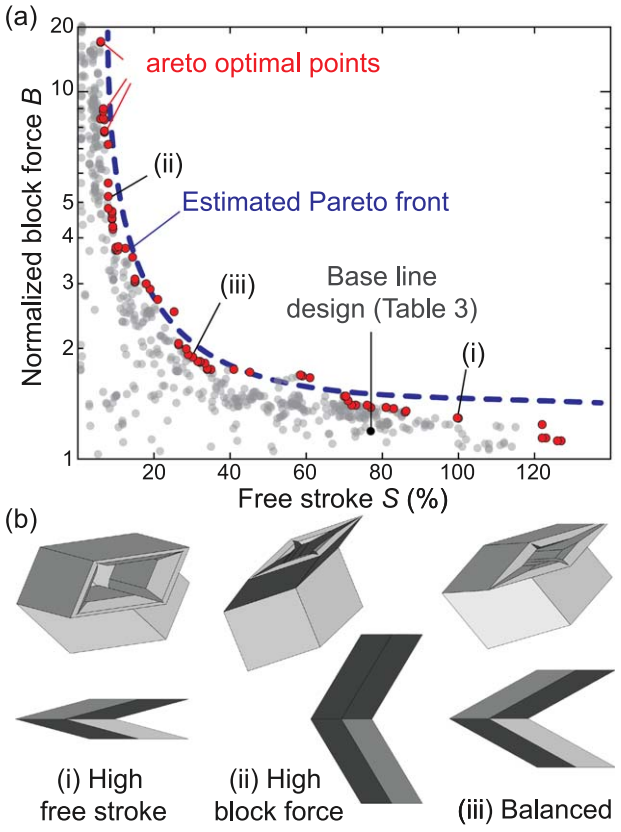

Figure 13. Results of the constrained genetic optimization. (a) Each gray dot represents the free stroke and block force performance of a feasible fluidic origami designs generated in the optimization iterations. The highlighted dots are the Pareto optimal results. (b) CAD rendering of the optimal designs with high free stroke, high block force, and a balanced performance, respectively.

issues. This constraint was reinforced by the SOLIDWORKS plugin, which automatically discards the geometrically incompatible designs. In addition, a requirement of $t_f > t_{C3}$ is reinforced during the design variable selection process. The second constraint is that the maximum stress from internal pressure should not exceed the material ultimate tensile strength. The ultimate strength of the 3D printed TPU materials are 80 MPa, and in this optimization, we introduce a safety factor of 2 and limit the maximum stress at 40 MPa. The optimization setup in modeFRONTIER is shown in A.2 of the appendix.

To ensure the global optimal is reached, the genetic optimization iterates for 25 generations and creates 658 valid designs, and the values of the corresponding objective functions are shown in figure 13. Due to the conflict relationship between these two objectives, no single optimized design is feasible. Instead, a Pareto front can be identified based on the 74 pareto-optimal design points identified by the modeFRONTIER. The distribution of design variables in these optimal designs are shown in table 5. The sector angle γ among the optimal designs shows a large variation. It is observed that γ in the range of 32° to 60° yield stronger free stroke performance, while those in the range of 60° to 86° yield a stronger block force performance. The corresponding resting folding angle $\theta°$ surprisingly shows a significantly

Table 5. The arithmetic mean and standard deviation of the design values among the Pareto optimal designs shown in figure 13.

Design Parameter		Mean	Deviation
Miura-ori backbone	γ	68.1°	18.0°
	$\theta°$	79.2°	1.4°
Additional design variables	t_F	4.5 mm	0.9 mm
	t_{C1}	1.3 mm	0.7 mm
	t_{C2}	1.4 mm	0.9 mm
	w_{C1}	3.3 mm	0.8 mm
	w_{C2}	3.4 mm	1.4 mm
	t_{C3}	1.3 mm	0.2 mm
	d_{C3}	3.6 mm	1.0 mm

smaller variation near the mean value of $\theta° = 79.2°$, which can be considered as the optimal folding angle for actuation. Therefore, we can conclude that the averaged values of the resting folding angle and crease thinning variables shown in table 5 are the optimal fluidic origami designs, meanwhile, tuning the sector angle γ is the most effective approach for tuning the actuation performance for specific application requirements (figure 13(b)).

6. Summary and conclusion

Via analytical investigation, finite element simulation, experiment validation, and design optimization, this study holistically examines the actuation performance of a plant-inspired fluidic origami cellular structure. In particular, we aim to understand the influences of thick facet material stiffness and pressure sealing end caps in order to obtain practical guidelines for implementing the fluidic origami. To this end, we construct CAD models of the fluidic origami modules based on realistic design parameters to ensure that they can be fabricated via commercially accessible 3D printers while remaining pressure proof. Two fluidic origami prototypes based on different designs, 3D printing methods, and materials are fabricated for experimental validation. We then use two different approaches to examine the free stroke and block force performance of fluidic origami. The first approach is to use simplified analytical models that assume zero facet thickness and ideal end caps. In particular, for free-stroke analysis we use a model based on rigid-folding kinematics; and for block force analysis we use an equivalent truss-frame model. These analytical models have been used extensively for the previous studies of origami applications. The second approach is to use the more comprehensive nonlinear finite element simulation. Comparing the results from these different approaches can reveal the influence of thick facet material stiffness and realistic end caps. It is found that the thick facets and end caps reduce the magnitude of free stroke and block force. They also alter the deformation pattern of fluidic origami under pressure. That is, in the free-stroke analysis, the end caps induce localized bending deformation at each end of the fluidic origami module; in the block force

analysis, the thick facet and end caps prevent the non-uniform elongation and contraction predicted by the truss-frame model. However, thick facet and end caps do not qualitatively change the relationships between the actuation performance and the underlying Miura-ori design.

Based on these insights, we developed a customized generic algorithm, based on the finite element model, to identify the optimal fluidic origami designs for actuation. We find an optimal resting folding angle to maximize the actuation capability, while the sector angle in Miura-ori can be tailored to effectively program the actuation performance. Therefore, this study provides the practical guidelines for implementing fluidic origami for many applications that require embedded actuation such as morphing airframe and soft robots.

Acknowledgments

H Sane, P Bhovad, and S Li acknowledge the supported from the National Science Foundation through Award # CMMI-1633952 and 1751449 (CAREER); and Clemson University through startup funding and Dean's Faculty Fellow Award.

Appendix

A.1. Equivalent stiffness parameter formulation

This section details the formulation used for defining the stiffness parameters used in this study: They are the equivalent crease torsional stiffness k_i^c, facet bending stiffness k_i^f, and facet stretching stiffness k_i^s, where the sub-index i identifies the different creases or facets in the fluidic origami module. The simplified free-stroke analysis section 3.1 uses only the crease torsional stiffness, while the truss-frame model in section 4.1 uses all three stiffness parameters. Much of the published work on such stiffness calculation is applicable to uniform thin sheets made of linearly elastic materials, but the fluidic origami modules are fabricated from 3D printed hyperelastic materials. Moreover, the fabricated modules feature v-grooves along the crease lines to facilitate proper folding. Currently, there is no universal framework to describe mechanical properties of such structures, so we resort to careful approximation techniques to describe these stiffness properties. In the subsections below, we present the stiffness parameter formulation which approximates the folding characteristics of the 3D printed fluidic origami as seen in the experiments and finite element analyses.

Crease torsional stiffness k_i^c :
The crease torsional stiffness characterizes the elastic folding and unfolding behaviors along the crease lines. To derive this parameter, we approximate the crease as a non-uniform cantilever beam subjected to an external moment M (figure 14). The magnitude of this moment is chosen such that it creates crease deformations of the same order as seen in finite element simulations. The applied moment is higher in the free-stroke analysis than in the block force analysis; because the crease folding is more significant in the former case. To simplify the analysis, we neglect the constraining effects due to surrounding facets so that the crease stiffness parameter is calculated based on the following equations:

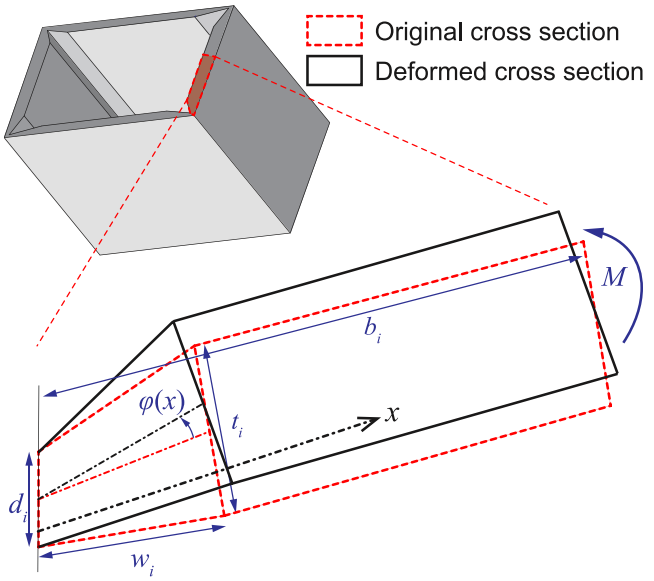

Figure 14. An example of the cross-section area of half of a crease, which is modeled as a non-uniform cantilever beam for crease torsional stiffness characterization.

$$k_i^c = \frac{M}{\varphi(w_i)}, \tag{8}$$

where the crease folding angle $\varphi(w_i)$ is related to the applied moment M and resting crease dihedral angle φ° is defined at the stress-free state:

$$\varphi(w_i) = \int_0^{b_i} \frac{M}{EI(x)} dx + \varphi^\circ, \tag{9}$$

and

$$I(x) = \begin{cases} \frac{1}{12} l_i \left(d_i + (t_i - d_i)\frac{x}{w_i} \right)^3 & 0 \leqslant x \leqslant w_i \\ \frac{1}{12} l_i {t_i}^3 & w_i \leqslant x \leqslant b_i \end{cases}. \tag{10}$$

The crease geometry parameters l_i, d_i, w_i, t_i, and b_i are chosen based on the 3D CAD designs shown in figure 3, tables 1, and 3. The ideal end caps are simulated by assigning zero crease stiffness at the boundary. Since the crease stiffness is a function of resting dihedral opening angle φ°, it is dependent on the Miura-ori resting folding angle θ°.

Facet bending stiffness k_i^f :
The facet bending stiffness is added to the truss elements that triangulates the facets in the equivalent truss-frame model (figure 9). The facet bending is not considered in the rigid-folding kinematics, but it's important to be taken into account for the fluidic modules fabricated from realistic materials. The 3D printed modules show notable facet bulging when the internal pressure is very high. To derive this stiffness

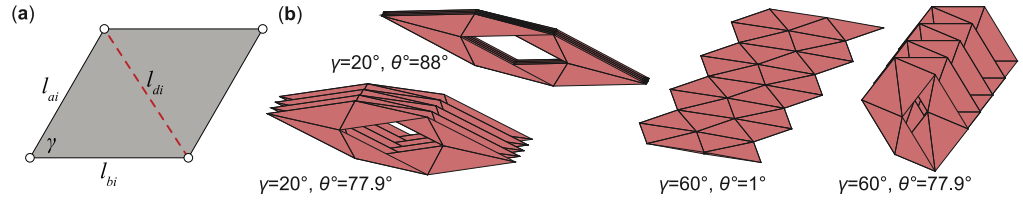

Figure 15. Estimating the facet bending and stretching stiffness. (a) The schematic diagram of a facet showing the truss-frame elements and geometric variables. (b) The four different examples of Miura-ori designs, and their corresponding stiffness parameters are summarized in table 6.

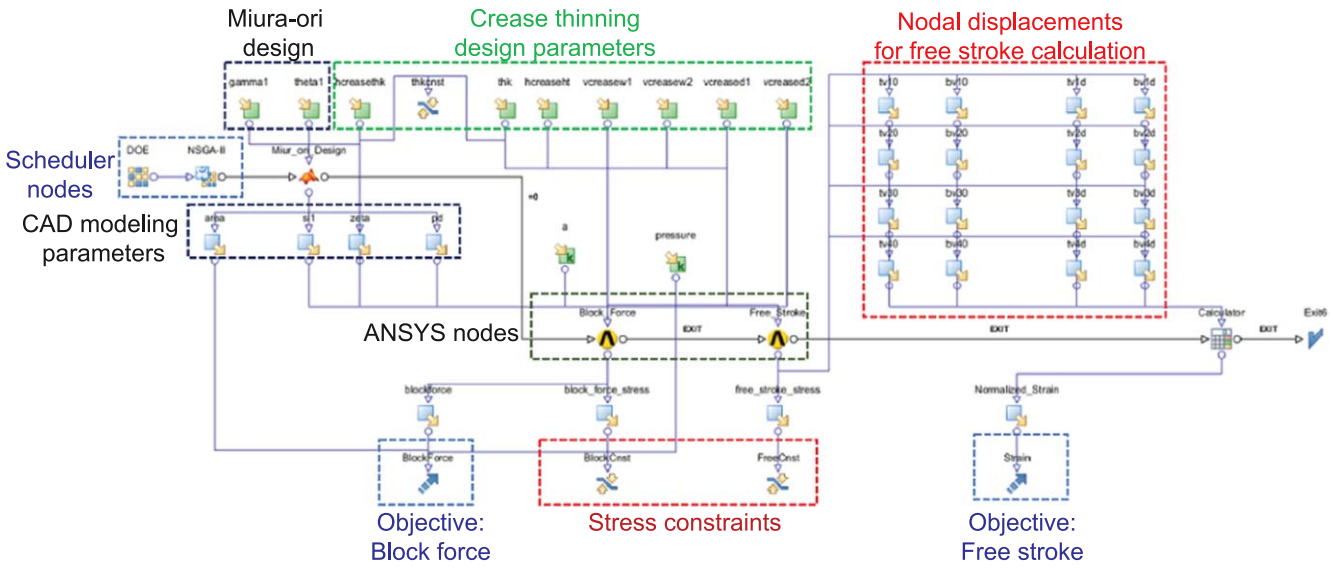

Figure 16. A screenshot of the modeFRONTIER optimizer used in this study.

Table 6. The normalized stiffness parameters of four examples of fluidic origami design shown in figure 15.

Stiffness	$\gamma = 20°, \theta° = 77.9°$	$\gamma = 20°, \theta° = 88°$	$\gamma = 60°, \theta° = 1°$	$\gamma = 60°, \theta° = 77.9°$
k^c/a	3.9	3.8	4.5	3.9
k^f/a	103.3	103.3	139.8	139.8
$k^s a$	$k_a^s = k_b^s = 1.4 \times 10^3$ $k_d^s = 8.5 \times 10^3$	$k_a^s = k_b^s = 1.4 \times 10^3$ $k_d^s = 8.5 \times 10^3$	$k_a^s = k_b^s = 1.4 \times 10^3$ $k_d^s = 3.4 \times 10^3$	$k_a^s = k_b^s = 1.4 \times 10^3$ $k_d^s = 3.4 \times 10^3$

parameter, we use the formulation introduced by Lobkovskey *et al* for small bending angle deformations (<0.1 radian) [34]. This assumption is consistent with the facet deformations seen in experiments and finite element simulation. We define a scaling parameter SF to ensure that the equivalent facet bending stiffness k_i^f is at least an order higher than the crease stiffness k_i^c so that

$$k_i^f = SF\frac{Et_{fi}^3}{12(1-\nu^2)}\left(\frac{l_{di}}{t_{fi}}\right)^{1/3}, \tag{11}$$

where the elastic modulus E is estimated based on the dog bone tests shown in figure 4, $\nu = 0.45$ is the Poisson's ratio, and t_{fi} is the facet thickness. Note that the facet bending stiffness is function of diagonal truss element length l_{di}, which in turn is related to the crease lengths a, b and facet sector angle γ.

Facet stretching stiffness k_i^s

The facet stretching stiffness is assigned to all of the truss elements in the truss-frame model. Filipov *et al* introduced a stretching stiffness formulation to model thin sheets in origami [6]. They assumed isotropic material properties and uniform sheet thickness to describe in-plane stretching and shearing behavior of initially unbent facets. We adopt the same formulation, which provides satisfactory results to qualitatively describe the fluidic origami actuator performance. The equivalent stretching stiffness k_i^s for the truss element is calculated by,

$$k_{ki}^s = E\frac{A_{ki}}{l_{ki}}, \tag{12}$$

where the sub-index $k = a$, b, or d represents the different

truss members in the facet #*i* (figure 15(a)), so that

$$A_{bi} = \frac{t_f(a^2 - \nu b^2)}{2a(1-\nu^2)},\ A_{ai} = \frac{t_f(b^2 - \nu a^2)}{2b(1-\nu^2)},$$
$$A_{di} = \frac{\nu t_f(a^2+b^2)^{1.5}}{2ab(1-\nu^2)}, \quad (13)$$

and

$$l_{bi} = b,\ l_{ai} = a,\ l_{di} = \sqrt{a^2 + b^2 - 2ab\cos(\gamma)}. \quad (14)$$

Thus, the stretching stiffness is inversely proportional to the length of truss elements. Based on the formulations above, we can calculate the stiffness parameters for every facet and crease, and use them for the parametric analysis of free-stroke and block force. Table 6 shows the calculated stiffness parameters corresponding to four different examples of Miura-ori designs (figure 15(b)). Results in this table clearly show the connection between the stiffness parameters and the Miura-ori designs. The crease folding stiffness k_i^c decreases when $\theta°$ increases. while change in γ doesn't have any effect on its value. The facet bending stiffness k_i^f increases when γ increases, while change in $\theta°$ doesn't have any effect on its value. The crease stretching stiffness k_a^s and k_b^s is independent of the changes in $\theta°$ and γ; while the facet stretching stiffness k_d^s decreases with an increasing γ.

A.2. modeFRONTIER optimizer set up

Figure 16 shows a screenshot of the modeFRONTIER optimizer developed for this study. The scheduler node in this optimizer comprises of the design of experiment (DOE) and the optimizing algorithm (NSGA-II). The values for crease thinning as well as the Miura-ori backbone design parameters γ and $\theta°$ are assigned by this node. The MATLAB node generates the CAD modeling parameters accordingly, and sends these parameters to the ANSYS nodes. Within the ANSYS nodes, a SolidWorks plugin builds the CAD model using these parameters and performs FEA simulations for free stroke and block force. Nodal displacements of vertices of both end caps are extracted from the free stroke FEA simulation to calculate the normalized free stroke in the calculator node. The objective nodes store the free stroke and block force performance, which are then used by the NSGA-II solver to generate new designs.

ORCID iDs

Priyanka Bhovad https://orcid.org/0000-0002-6934-2151
Suyi Li https://orcid.org/0000-0002-0355-1655

Reference

[1] Lang R J 1996 A computational algorithm for origami design *Annual Symp. on Computational Geometry (SCG)* (New York, New York, USA: ACM Press) pp 98–105
[2] Demaine E D and O'Rourke J 2007 *Geometric Folding Algorithms: Linkages, Origami, Polyhedra* (New York, NY, USA: Cambridge University Press)
[3] McArthur M and Lang R J 2013 *Folding paper: The Infinite Possibilities of Origami* (Rutland, VT, USA: Tuttle Publishing)
[4] Zirbel S A, Lang R J, Thomson M W, Sigel D A, Walkemeyer P E, Trease B P, Magleby S P and Howell L L 2013 Accommodating thickness in origami-based deployable arrays *J. Mech. Des.* **135** 111005
[5] Schenk M, Viquerat A D, Seffen K A and Guest S D 2014 Review of inflatable booms for deployable space structures: packing and rigidization *J. Spacecr. Rockets* **51** 762–78
[6] Filipov E T, Tachi T and Paulino G H 2015 Origami tubes assembled into stiff, yet reconfigurable structures and metamaterials *Proc. Natl. Acad. Sci.* **112** 12321–6
[7] Chen Y, Peng R and You Z 2015 Origami of thick panels *Science (80-.)* **349** 396–400
[8] Felton S, Tolley M, Demaine E D, Rus D and Wood R 2014 A method for building self-folding machines *Science (80-.)* **345** 644–6
[9] Miyashita S, Guitron S, Ludersdorfer M, Sung C R and Rus D 2015 An untethered miniature origami robot that self-folds, walks, swims, and degrades *2015 IEEE Int. Conf. on Robotics and Automation (ICRA)* vol 2015–June (Seattle, USA: IEEE) pp 1490–6
[10] Johnson M, Chen Y, Hovet S, Xu S, Wood B, Ren H, Tokuda J and Tse Z T H 2017 Fabricating biomedical origami: a state-of-the-art review *Int. J. Comput. Assist. Radiol. Surg.* **12** 2023–32
[11] Schenk M and Guest S D 2013 Geometry of Miura-folded metamaterials *Proc. Natl. Acad. Sci.* **110** 3276–81
[12] Overvelde J T B, Weaver J C, Hoberman C and Bertoldi K 2017 Rational design of reconfigurable prismatic architected materials *Nature* **541** 347–52
[13] Fang H, Li S, Ji H and Wang K W 2016 Uncovering the deformation mechanisms of origami metamaterials by introducing generic degree-four vertices *Phys. Rev.* E **94** 043002
[14] Wang P, Meyer T A, Pan V, Dutta P K and Ke Y 2017 The beauty and utility of DNA origami *Chem.* **2** 359–82
[15] Tachi T 2010 Freeform variations of origami *J. Geom. Graph.* **14** 203–15
[16] Dudte L H, Vouga E, Tachi T and Mahadevan L 2016 Programming curvature using origami tessellations *Nat. Mater.* **15** 583–8
[17] Li S and Wang K W 2015 Fluidic origami: a plant-inspired adaptive structure with shape morphing and stiffness tuning *Smart Mater. Struct.* **24** 105031
[18] Forterre Y 2013 Slow, fast and furious: understanding the physics of plant movements *J. Exp. Bot.* **64** 4745–60
[19] Dumais J and Forterre Y 2012 'Vegetable dynamicks': the role of water in plant movements *Annu. Rev. Fluid Mech.* **44** 453–78
[20] Gramüller B, Köke H and Hühne C 2015 Holistic design and implementation of pressure actuated cellular structures *Smart Mater. Struct.* **24** 125027
[21] Vos R and Barrett R 2011 Mechanics of pressure-adaptive honeycomb and its application to wing morphing *Smart Mater. Struct.* **20** 094010
[22] Vasista S and Tong L 2013 Topology-optimized design and testing of a pressure-driven morphing-aerofoil trailing-edge structure *AIAA J.* **51** 1898–907
[23] Li S and Wang K W 2017 Plant-inspired adaptive structures and materials for morphing and actuation: a review *Bioinspir. Biomim.* **12** 011001
[24] Li S and Wang K W 2015 Fluidic origami with embedded pressure dependent multi-stability : a plant inspired innovation *J. R. Soc. Interface* **12** 20150639

[25] Forterre Y, Skotheim J M, Dumais J and Mahadevan L 2005 How the Venus flytrap snaps *Nature* **433** 421–5
[26] Vasista S, Tong L and Wong K C 2012 Realization of morphing wings: a multidisciplinary challenge *J. Aircr.* **49** 11–28
[27] Laschi C, Mazzolai B and Cianchetti M 2016 Soft robotics: Technologies and systems pushing the boundaries of robot abilities *Sci. Robot.* **1** eaah3690
[28] Tsuchiya T, Kameyama K, Kishi Y, Yoshimura M, Kanzawa N and Sameshima M 2000 Tyrosine phosphorylation in plant bending *Nature* **407** 37–37
[29] Eidini M and Paulino G H 2015 Unraveling metamaterial properties in zigzag-base folded sheets *Sci. Adv.* **1** e1500224–1500224
[30] Li S, Fang H and Wang K W 2016 Recoverable and programmable collapse from folding pressurized origami cellular solids *Phys. Rev. Lett.* **117** 114301
[31] Tachi T 2011 Rigid foldable thick origami *Origami 5* vol 5 ed P Wang-Iverson, R J Lang and M Yim (Boca Raton, FL, USA: A K Peters/CRC Press) pp 253–64
[32] Gramüller B, Tempel A and Hühne C 2015 Shape-variable seals for pressure actuated cellular structures *Smart Mater. Struct.* **24** 095005
[33] Filipov E T, Liu K, Tachi T, Schenk M and Paulino G H 2017 Bar and hinge models for scalable analysis of origami *Int. J. Solids Struct.* **124** 26–45
[34] Lobkovsky A, Gentges S, Li H, Morse D and Witten T A 1995 Scaling properties of stretching ridges in a crumpled elastic sheet *Science (80-.)* **270** 1482–5